RSC Advances

ROYAL SOCIETY OF CHEMISTRY

www.rsc.org/advances

Cite this: DOI: 10.1039/c0xx00000x

www.rsc.org/xxxxxx

ARTICLE TYPE

Local structure of low-temperature γ-Al_2O_3 phases as determined by the luminescence of Cr^{3+} and Fe^{3+}

Alexander Rastorguev,*[a] Mark Baronskiy[a], Aleksey Zhuzhgov[a], Anton Kostyukov[a], Oleg Krivoruchko[a] and Valeriy Snytnikov[b]

Received (in XXX, XXX) Xth XXXXXXXXX 20XX, Accepted Xth XXXXXXXXX 20XX
DOI: 10.1039/b000000x

The γ and γ* phases of alumina synthesized from crystalline boehmite and pseudoboehmite were shown to strongly differ in some physicochemical characteristics. Photoluminescence of Cr^{3+} and Fe^{3+} as luminescent probes with their natural impurity concentrations was detected in the tested alumina samples and the local structure of the samples was examined. The crystal field strength and Racah parameters in γ-Al_2O_3 phases were determined. The ratio of octahedral and tetrahedral cationic positions was equal to 1 for γ-Al_2O_3 synthesized from crystalline boehmite, and 0.3 for that obtained from pseudoboehmite. The effect of residual OH groups and weakly bound molecular water on the local structure of γ-Al_2O_3 phases was revealed. The luminescence of Cr^{3+} was detected in subsurface structures of each alumina; defects produced by nanocrystallites were shown to affect the luminescence.

Introduction

Aluminas are among the widely used inorganic compounds. In chemical processes, aluminas are employed as adsorbents, catalyst supports and catalysts. [1-3]

Polymorphous modifications of alumina (η-, γ-, χ-, δ-, θ- and α-Al_2O_3) have identical composition but different crystal structures. The best studied is the thermodynamically stable high-temperature α-Al_2O_3 phase (corundum). In its rhombohedral lattice, cations have the octahedral surroundings of anions. The low-temperature species (η- and γ-Al_2O_3) possess a cubic lattice with the defect spinel structure, which is formed during the alumina synthesis. The structure and defectness of these lattices depend on the properties of starting aluminum hydroxides (AH), their impurity content, and synthesis conditions of the final oxides.[4] As shown by the X-ray diffraction studies, the structure of γ-Al_2O_3 differs in the coherent scattering lengths depending on the starting hydroxide (boehmite or pseudoboehmite) that is chosen as a precursor substance.[5-7]

For catalysis and many other applications, it is essential to elucidate the local structure of alumina at the level of ion bond lengths. The luminescence analysis methods are promising for this purpose. The presence of "structurally sensitive" ions in alumina allows obtaining the electronic luminescence spectra of these ions in the alumina matrix. The analysis of such spectra can reveal features of the alumina local structure, particularly the phase composition of the alumina matrix. In works[8-12], the local structure of aluminas, including γ-Al_2O_3, was examined with the use of Cr^{3+} ions; aluminas were doped with these ions during the synthesis. However, such doping may change the crystal structure of the starting alumina. Applicability of the results obtained in these works to other low-temperature alumina samples is strongly limited by the absence of data on the effect of a precursor substance on the luminescence of Cr^{3+} in alumina. At the same time, chromium, iron and other elements can be present in low concentrations as the "concomitant impurities" even in high-purity aluminas.[12-14] The luminescence capability of Cr^{3+} ion in alumina and the availability of detailed information on the electronic structure of this ion distinguish Cr^{3+} from other spectroscopic probes. Fe^{3+} ion is less convenient but also applicable for luminescence probing. The use of Cr^{3+} and Fe^{3+} as probes in their natural concentrations makes it possible to exclude special modification of alumina samples; so, no additional distortions are introduced in the system under consideration. Thus, the Cr^{3+} and Fe^{3+} concomitant impurity cations can be considered as luminescent probes for revealing a relation between spectral-luminescence properties of the activator and the local structure of alumina.

The goal of this work was to elucidate the local structure of bulk and subsurface regions of the single-phase γ- and γ*- Al_2O_3 powders, synthesized from crystalline boehmite (BE) and pseudoboehmite (P/BE), with the use of Cr^{3+} and Fe^{3+} luminescent probes present in a concentration of the concomitant impurity.

Experimental

Comprehensive thermogravimetric analysis (TGA) of the synthesized AH was performed on a NETZSCH TGA instrument (Germany) over the temperature range from 20 to 1000 °C at a heating rate of 10 °C/min using the 30 mg samples.

The total water content in samples under investigation was found from the weight loss upon calcination of the samples in the temperature range from 550 to 1250 °C.

Elemental chemical analysis of the samples was carried out by

the X-ray fluorescence method on an ARL – Advant'x analyzer with a Rh anode of the X-ray tube. The detection limit of the instrument was 0.01 wt.%.

X-ray diffraction analysis (XRD) of the samples was performed on a Siemens D-500 diffractometer with CuK_α radiation and a reflected beam graphite monochromator. Diffraction patterns of the samples were recorded by scanning over the 2θ angular range of 10-70° with a step of 0.05° and accumulation time of 3 s. Phases were identified by comparing the experimental diffraction patterns with those from ICDD PDF 2 database.

Morphology of the samples was characterized by high resolution transmission electron microscopy (HRTEM) on a JEM-2010 microscope at accelerating voltage 200 kV and resolution 1.4 Å. The samples were deposited on a copper grid by dispersing the solid phase powder in alcohol with an ultrasonic disperser.

Photoluminescence (PL) spectra and photoluminescence excitation (PLE) spectra were measured on a CaryEclipse (Varian) spectrofluorimeter. Spectrofluorimeter equipped with a Xenon flash lamp with the peak pulse power of 75 kW. The measurement range of PL spectra was 550 – 900 nm; PLE spectra were recorded in the region of 350 – 700 nm. Samples were placed in a quartz cell and frontal irradiation with minimization of reflected light was employed. PL spectra were corrected for the spectral distribution of photomultiplier sensitivity, and PLE spectra – for the wavelength distribution of lamp intensity. All the measurements were made at room temperature. PL and PLE spectra of all the cells were measured to consider their possible contribution to the spectra of the test samples. We have not seen any signs of deviation from the linearity in spectra obtained.

Sample preparation

Two modifications having different X-ray diffraction properties, γ- and γ*-Al_2O_3, were synthesized by heat treatment of crystalline boehmite (L-1) and pseudoboehmite (L-2) in air at 550 °C for 4 h.

Crystalline boehmite (γ-AlOOH) was obtained by hydrothermal treatment of γ-$Al(OH)_3$ (gibbsite) in a stainless steel autoclave at 250 °C in saturated water vapor. Pseudoboehmite AH was synthesized by simultaneous pouring of equinormal aqueous (distillate) solutions of $Al(NO_3)_3 \times 9H_2O$ salt and ammonium hydrocarbonate at a constant pH = 7.0. To obtain a pseudoboehmite sediment, the mixed solutions were held at 80 °C for 2 h. The resulting AH sediment was separated from the aqueous solution by decanting, washed from impurities with distilled water, and dried in an air flow at 150 °C for 12 h to a constant weight. All the reagents were of analytical grade.

The α-Al_2O_3 powders were obtained from each structural modification of alumina by calcination in air at 1250 °C for 4 h. The α-Al_2O_3 samples synthesized from L-1 and L-2 are denoted as L-3 and L-4, respectively.

As shown by the comprehensive thermogravimetric analysis, the starting boehmite is characterized by the endothermic effect at 550 °C, which is caused by dehydration of the boehmite and its phase transition to the γ-Al_2O_3 crystal modification (Fig. 1a). Therewith, the total weight (water) loss is 13.88%, which virtually corresponds to a theoretical value of 15% calculated by the equation:

$$2AlOOH \rightarrow Al_2O_3 + H_2O$$

Three thermal effects are distinguished in a thermogram of pseudoboehmite (Fig. 1b): a broad endothermic effect with a maximum at 97 °C, which is due to the removal of weakly bound molecular water; the main endothermic effect at 381 °C, indicating the dehydration of P/BE (the removal of structural OH groups) and its phase transition to γ*-Al_2O_3; and the exothermic effect at 290 °C caused by decomposition (dissociation) of an ammonium nitrate impurity that was produced in the early steps of P/BE synthesis (the weight loss after its removal is 34.52%). The total weight loss for the synthesized sample is 54.93% (Fig. 1b). The value obtained by subtraction of the weight loss related to decomposition of NH_4NO_3 will correspond to the total water content (in the molecular form and as the OH groups) in P/BE. Thus, according to TGA data, the weight losses upon calcination particularly for P/BE are equal to 20.41% and a gross chemical formula for this hydroxide can be written as $AlOOH \times 0.37H_2O$. It should be noted also that temperature of the P/BE phase transition to γ*-Al_2O_3 is 170 °C lower as compared to crystalline boehmite, thus indicating a disordered (labile) state of the pseudoboehmite system.

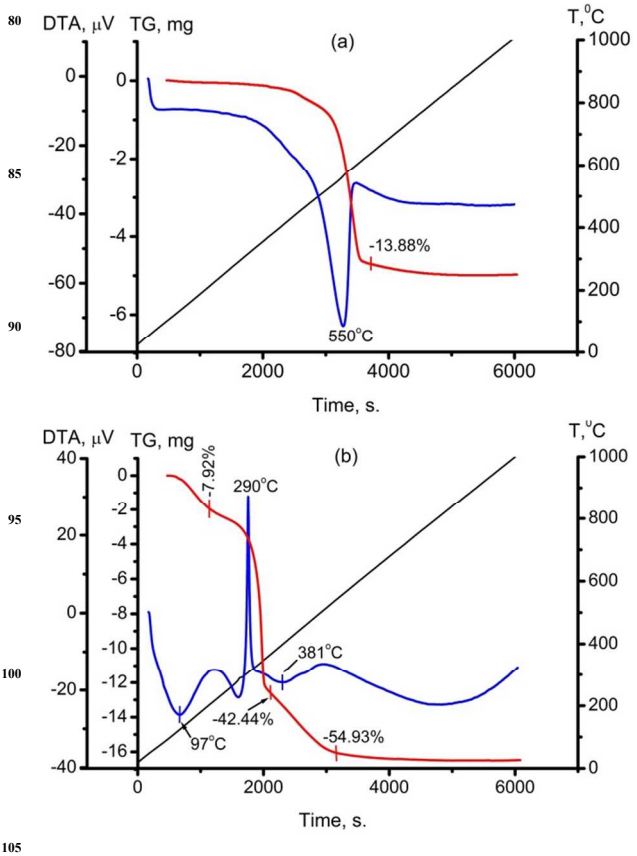

Fig.1 Comprehensive thermogravimetric analysis (losses in wt.%): a – crystalline BE; b – P/BE.

γ-Al_2O_3 (L^E), obtained by centrifugal thermal activation (CTA) of gibbsite[15], was used as the reference sample to estimate chromium and iron concentrations in L-1 and L-2 samples using PL. In the L^E sample, the concentration of chromium and iron is 0.006 and 0.008 wt.%, respectively.[15] Chromium concentration in L-3 and L-4 samples was estimated from PL using a ruby single crystal (Cr^{3+}:α-Al_2O_3, Cr^{3+} concentration 0.01 wt.%).[15]

Table 1 lists the phase composition of the starting AH and their calcination products as well as the heat treatment conditions.

Table 1. Phase composition (PC) of the starting and target compounds; heat treatment conditions.

Target samples	PC of starting aluminum hydroxides and oxides	$T_{synthesis}$, °C/$t_{calcination}$, h	PC of target aluminas
L-1	BE	550/4	γ-Al_2O_3
L-2	P/BE		γ*-Al_2O_3
L-3	γ-Al_2O_3	1250/4	α-Al_2O_3
L-4	γ*-Al_2O_3		α*-Al_2O_3

* - Aluminas obtained by heat treatment of pseudoboehmite

Results

Data of the elemental analysis are listed in Table 2. Chromium and iron contents in the samples are below the detection limit of the X-ray fluorescence spectroscopy.

Table 2. Content of elements in L-1 and L-2 samples (wt.%).

Sample	Si	Ti	Ca	K	Cu	P	Cl	Ni
L-1	0.23	0.06	0.02	0.03	0.01	0.01	-	-
L-2	0.05	-	0.01	-	-	-	0.02	0.01

In compliance with the ICDD PDF 2 database, the diffraction patterns of the starting AH testify to their single-phase nature (Fig. 2).

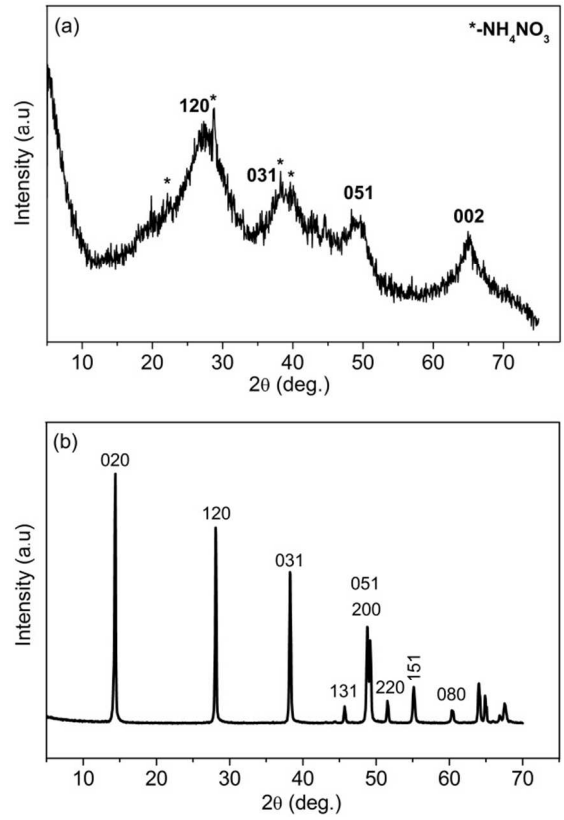

Fig.2 Diffraction patterns of the starting AH: a – P/BE (without the 020 reflection); b – BE.

Note that the diffraction pattern theoretically calculated for crystalline BE according to[7] is identical with the curve obtained in our experiment (Fig. 2b). The diffraction pattern of P/BE shows also the reflections from ammonium nitrate, which was formed during the synthesis and could not be removed completely by washing the sediment, which agree with the TGA data (Fig. 1b).

As shown by XRD, L-1 and L-2 samples have the developed crystal structures (Fig. 3, curves 1, 2). One can see from the diffraction patterns that in the case of L-2 the positions of maxima for the observed {400} and {440} reflections are identical to those for L-1. Therewith, their broadened base indicates a stronger disordering of the oxygen lattice in L-2 as compared to L-1. In comparison with the starting compound (Fig. 2a), the reflections from NH_4NO_3 are absent in the diffraction pattern of sample L-1, thus testifying to its full decomposition during the heat treatment.

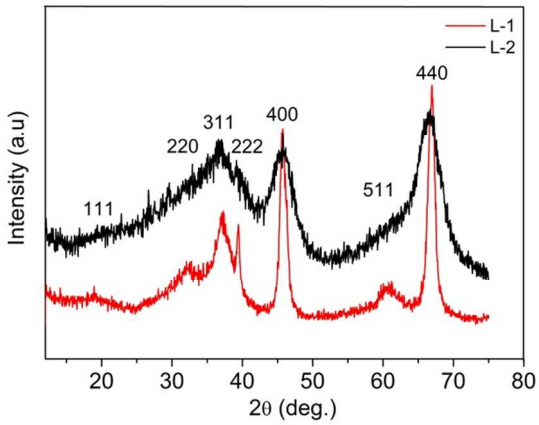

Fig.3 Diffraction patterns of L-1 and L-2 samples.

According to HRTEM data, the morphology of L-1 sample is characterized by the presence of large lamellar 3D single crystallites, their size ranging from 100 nm to some microns (Fig. 4 a). In its turn, L-2 sample consists of mutually disordered nanocrystallites with the diameter of 10-15 nm, which constitute polycrystal micron-size aggregates (Fig. 4 b, c).

An additional calcination of L-1 and L-2 samples at 550-1250 °C, resulting in the formation of the α-Al_2O_3 phase, showed that the content of water (mostly the bulk and surface impurity OH groups not removed earlier) was 4.3 wt.% for L-1 and 14.2 wt.% for L-2.

According to measurements, the specific surface area (S_{sp}) of L-1 sample was 85 m^2/g, while that of L-2 was substantially higher, 241 m^2/g.

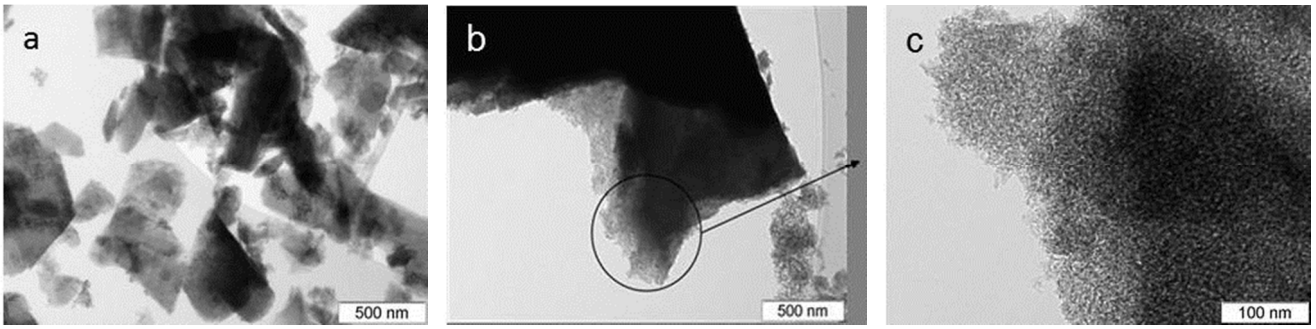

Fig.4 TEM images of samples L-1 (a) and L-2 (b, c).

Results of luminescence studies

The starting AH – crystalline boehmite and pseudoboehmite – showed no luminescence at room temperature. PL typical of Cr^{3+}:α-Al_2O_3 (Fig. 5b) and PLE spectra (Fig. 5a) were obtained for samples L-3 and L-4.

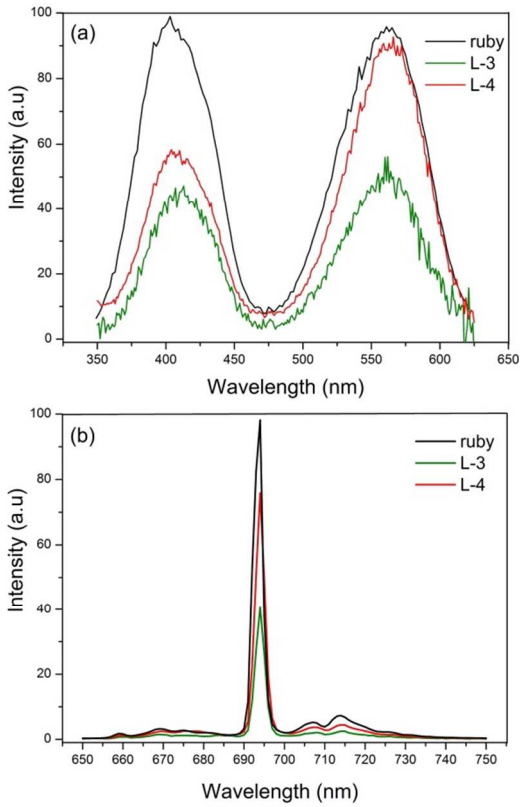

Fig. 5 PLE (a) and PL (b) spectra of L-3, L-4 and ruby single crystal. λ_{ex} = 530 nm.

The resolution of spectrofluorimeter was not sufficient to distinguish the characteristic R_1 and R_2 lines of Cr^{3+}:α-Al_2O_3 (the $^2E \rightarrow {}^4A_2$ transition). So, in the PL spectrum these lines merge into a single line with a maximum at λ_{max} = 694 nm (Fig. 5 b).[10,11] In the PL spectrum, a set of less intense lines is observed in the Stokes and anti-Stokes regions at λ_{max} = 659, 669, 676, 707 and 714 nm (Fig. 5b). PLE spectra of L-3 and L-4 showed the bands commonly attributed to Cr^{3+}:Al_2O_3, respectively, with the maxima at λ_{max} = 407, 409 nm and λ_{max} = 562, 563 nm (Fig. 5a). These bands correspond to $^4T_2 \rightarrow {}^4A_2$ and $^4T_1 \rightarrow {}^4A_2$ transitions.[15, 16] Spectra of L-3, L-4 and ruby single crystal recorded under identical conditions are compared in Fig. 5a, b.

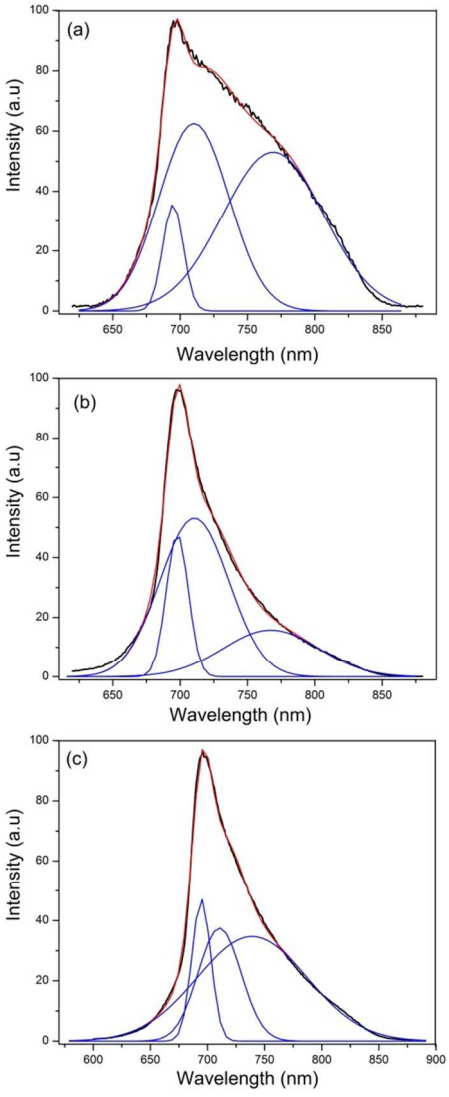

Fig.6 PL spectra for different samples: a – L-1, b – L-2, c – L^E, and Gaussian components. λ_{ex} = 530 nm.

For L-1 and L-2 samples, PL was detected in the region of 600 – 850 nm upon excitation at λ_{ex} = 530 nm. The PL spectra of L-1 and L-2 and their decomposition into Gaussian components are displayed in Fig. 6a, b. Fig. 6b shows the luminescence spectrum of the reference sample L^E. Two Gaussian components of PL spectra decomposition (Fig. 6) are attributed to the luminescence of Cr^{3+} ions, while the third component with a greater wavelength corresponds to Fe^{3+}. The attribution of components is substantiated below.

Chromium and iron contents in L-1 – L-4 samples were estimated quantitatively taking into account that PL spectra for all the samples – L^E, ruby, L-1, L-2, L-3, and L-4 – were measured under identical conditions. The obtained concentrations of chromium and iron are listed in Table 3.

Table 3. Calculated concentrations of chromium and iron in the samples (wt.%).

Sample	Chromium concentration	Iron concentration
L-1	0.4×10^{-4}	1.3×10^{-4}
L-2	2.1×10^{-4}	1.4×10^{-4}
L-3	1.9×10^{-4}	-
L-4	9.8×10^{-4}	-

PLE spectra of L-1 and L-2 samples were measured for the maxima of luminescence bands and compared with each other with respect to their intensities, the chromium content being taken into account (Fig. 7).

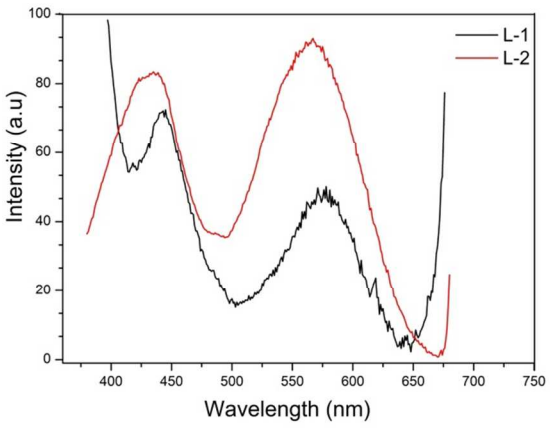

Fig.7 PLE spectra for samples L-1 (λ_{max} = 698 nm) and L-2 (λ_{max} = 696 nm, the intensity is reduced by a factor of 4).

Discussion

Experimental diffraction patterns (Fig. 2) of the P/BE sample synthesized in our work (without the 020 reflection) and BE generally agree with the available literature data. P/BE without the 020 reflection is the most disordered system in comparison with pseudoboehmite and crystalline boehmite.[5, 6] Various physicochemical methods (XRD, REDD – radial electron density distribution, and HRTEM) were employed in[5, 7, 17-19] to reveal the structural features of boehmites synthesized by different techniques, in particular, for the samples similar to those used in our study (see Fig. 2). The REDD method made it possible to demonstrate[7] that distances between atoms belonging to different layers decrease when going from crystalline BE to P/BE (without the 020 reflection). In the structure of such P/BE, a decrease in the crystal size increases the Al – O distance (from 2.04 to 2.30 Å) and decreases the Al – OH distance (from 1.89 to 1.80 Å) in the octahedral plane. Modeling the diffraction patterns of highly dispersed substances was used to elucidate the local structure of AH under consideration.[5, 7] The best fit to experimental diffraction pattern of P/BE (without the 020 reflection) was observed with the model of a thin wafer (one cell along the y axis). In this case, such P/BE comprises ~1000 Å aggregates consisting of disordered lamellar particles with 1-3 layers.[5] Exactly the small number of layers in such particles makes it difficult to examine experimentally the ordering of P/BE crystal structure (without the 020 reflection).

The diffraction patterns of samples L-1 and L-2 (Fig. 3) obtained in experiments correspond to the γ-Al_2O_3 phases according to XRD database ICID PDF 2 and coincide with the diffraction curves of γ-Al_2O_3 synthesized from BE and P/BE in the known works.[18, 19] In the literature, crystalline γ-Al_2O_3 is often identified with the alumina which is also denoted as "γ-Al_2O_3" but is obtained by heat treatment of pseudoboehmite (the gel-like boehmite).[19] However, these two products radically differ in their physicochemical and structural properties. In distinction to γ*-Al_2O_3, crystalline γ-Al_2O_3 has a defect spinel structure and is described by crystallochemical formula $Al_8[\square_{2.67}Al_{13.33}]O_{32}$.[1, 2, 17-19] It is seen that crystalline γ-Al_2O_3 contains Al^{3+} ions in tetrahedral (Al^{3+}_{Td}) and octahedral (Al^{3+}_{Oh}) oxygen surroundings, while cationic vacancies – mostly in the Al^{3+}_{Oh} positions.

PL spectra of L-1 (Fig. 6a), L-2 (Fig. 6b) and L^E (Fig. 6c) samples are located in the same spectral range, strongly differ in their shape and are represented by broad asymmetric bands with the maxima at λ_{max} = 696, 698 and 695 nm, respectively. All these spectra exhibit similar changes in the intensity: a sharp increase in luminescence and a gradual decrease toward higher wavelengths. The decrease in intensity of PL spectra in the region of 700-850 nm is different for L-1 and L-2 samples. The shape of the spectra is obviously nonelementary.

After estimating the chromium and iron contents in the samples, the spectra can be compared with respect to their intensity, which is demonstrated in Fig. 8.

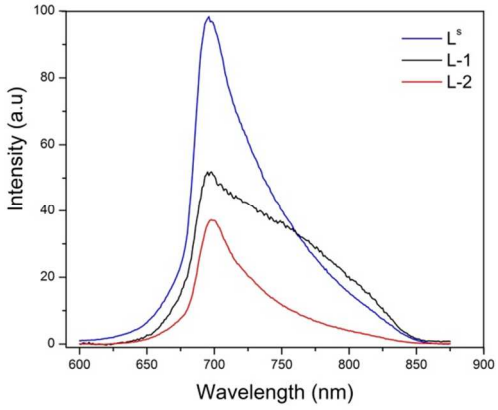

Fig. 8 PL spectra of L-1, L-2, and L^E samples with comparable concentrations of Cr^{3+}. PL intensity of the reference sample L^E is reduced by a factor of 9.5. λ_{ex} = 530 nm.

As follows from the spectra in Fig. 8, the integrated intensity

of PL for L-1 is 1.5-fold higher as compared to that of L-2. However, the content of residual impurity OH groups in L-2 is 3.3-fold higher than that in L-1. If the difference in PL intensities is caused by the quenching effect of residual OH groups, such groups are likely incorporated into the coordination sphere of chromium ions.

The decomposition of PL spectra (Fig. 6a, b, c) into Gaussians for each of L-1, L-2 and L^E samples is adequately approximated by three curves. This is confirmed by the virtual similarity of the envelope and experimental curves. Results of the decomposition into Gaussian components for L-1, L-2 and L^E samples are shown in Table 4.

Table 4. Maximum wavelengths and half-widths of Gaussian components for decomposition of luminescence spectra of L-1, L-2 and L^E samples.

L-1, λ_{max} / nm	$\Delta\lambda$ (L-1) / nm	L-2, λ_{max} / nm	$\Delta\lambda$ (L-2) / nm	L^E, λ_{max} / nm	$\Delta\lambda$ (L^E) / nm
λ_{a1} = 694.7	15.3	λ_{a2} = 697.8	16.4	λ_{a3} = 694.6	16.5
λ_{b1} = 709	52.1	λ_{b2} = 710.6	51.1	λ_{b3} = 710.6	37.5
λ_{c1} = 769.1	74.9	λ_{c2} = 767.4	71.1	λ_{c3} = 769	96.3

Note that each of the maxima at λ_{max} = 696, 698 and 695 nm, as it follows from decomposition into Gaussian components, is represented by superposition of two closely located curves (λ_{a1} = 694.7; λ_{b1} = 709) nm and (λ_{a2} = 697.8; λ_{b2} = 710.6) nm for L-1 and L-2, respectively (Table 4). One can see from the decomposition that PL of the samples in the region of 600 – 850 nm may be caused not only by emission of the Cr^{3+} cations but also by other 3d elements.[9-14, 20] As follows from the crystal field theory, the crystal field stabilization energy (CFSE) for d^3 (Cr^{3+}) configuration is maximal in the case of octahedral surrounding. This is why the Cr^{3+} cations are located mainly in the octahedra. It seems natural to relate the decomposition bands for L-1 (λ_{a1} = 694.7 nm, λ_{b1} = 709 nm), L-2 (λ_{a2} = 697.8 nm, λ_{b2} = 710.6 nm) and L^E (λ_{a3} = 694.6 nm, λ_{b3} = 710.6 nm) to the d-d transitions in Cr^{3+}:γ-Al_2O_3 (Fig. 6). L^E sample consists mostly of the γ-phase; the content of other impurities (χ-Al_2O_3) does not exceed 5%.[15, 21] Chromium content in L^E sample is by an order of magnitude higher than that in L-1 and L-2. Thus, the bands at λ_{a3} = 694.6 nm and λ_{b3} = 710.6 nm, taking into account the ratio of their areas, cannot correspond to chromium transitions in the phases other than γ-phase. The luminescence at λ_{a3} = 694.6 nm and λ_{b3} = 710.6 nm is not a splitting of R lines, because this range is much greater than 29 cm^{-1}. Thus, each of the bands corresponds to a certain type of the Cr^{3+} octahedral sites with different extent of distortion. The band at λ_{a1} = 694.6 nm is most close to the position of R lines in the α-phase, i.e., the $^2E \rightarrow {}^4A_2$ transition (a perfect octahedron). A broader band at λ_{b3} = 710.6 nm can be assigned to the $^4T_2 \rightarrow {}^4A_2$ transition. Such a transition may occur at substantial distortions of the octahedron when the $^4T_2$ level in a Tanabe-Sugano diagram corresponds to lower energies as compared to the ^2E level.

In alumina, emission of Fe^{3+} in the tetrahedral surroundings is commonly centered in a range of 740-770 nm[9, 12, 22], while Fe^{3+} in the octahedral surroundings is not emitted in this range. For $3d^5$ configuration, CFSE has such values that the octahedral and tetrahedral positions of Fe^{3+} ions become equiprobable.[16, 23] So, Gaussian components with the maxima at λ_{c1} = 769.1 nm, λ_{c2} = 767.4 nm and λ_{c3} = 769 nm for samples L-1, L-2 and L^E correspond to the occurrence of Fe^{3+} exactly in the tetrahedral positions. Additional evidence is the absence of the band at 740-770 nm in PL spectra (Fig. 5b) of the α-phase samples L-3 and L-4, which are virtually free of the tetrahedral positions.

Spectral resolution of the spectrofluorimeter was insufficient to obtain the excitation spectra for each Gaussian for samples L-1, L-2 and L^E. PLE spectra (Fig. 7) for L-1 (λ_{max} = 696 nm) and L-2 (λ_{max} = 698 nm) show broad bands in two regions: "blue" (350 – 500 nm) and "green" (475 – 650 nm). For L-1 and L-2, in the indicated wavelength regions one can see close but not coinciding bands with the maxima at λ_{max} = 443 and 575 for L-1 (Fig. 7, curve 2) and λ_{max} = 432 and 565 for L-2 (Fig. 7, curve 1). PLE spectra (Fig. 7) are similar to the excitation spectra of L-3, L-4 and single crystal (Fig. 5a) for which the corresponding bands are assigned to $^4T_2$ and $^4T_1$ states. There are differences in the positions of the maxima, intensities and half-widths. One can see from Table 4 and Fig. 6a, b, c that in L-1 each of the λ_{a1} and λ_{b1} maxima is shifted toward higher wavelengths in comparison with the position of non-split $R_{1,2}$ line corresponding to the transition of Cr^{3+} in the α-Al_2O_3 phase. This indicates a lower crystal field strength (10Dq) for these local positions of Cr^{3+}. The λ_{a2} and λ_{b2} maxima for L-2 (Fig. 6b) are shifter to a greater extent; for these positions of Cr^{3+} the crystal field strength should be even lower.

The results obtained can be analyzed using the crystal field theory. Cr^{3+} has a regular octahedral surrounding in the α-phase; the d-d transitions are well explained in the strong crystal field approximation. Distortions of the nearest surroundings of chromium ion are observed spectroscopically in the $^4T_2$ and $^4T_1$ positions and in the position of $R_{1,2}$ line maximum. In the spectra, the values of respective maxima of the Gaussian components (λ_{a1} = 694.7 nm and λ_{a2} = 697.8 nm) (Fig. 6a, b) do not coincide with the values obtained for the single crystal and annealed samples L-3 and L-4 (Fig. 5a, b). It means that the octahedral surroundings of Cr^{3+} in L-1 and L-2 samples are distorted. The distortions can be accounted for by estimating the crystal field strength. The calculation can be made using semiempirical expression (1)[23] and equations that describe the energies of $^4A_2$ and ^2E states of d^3 configuration in the cubic octahedral field, which are expressed (2-3) in terms of the Racah parameters (A, B and C).[24, 25]

$$B = \frac{\delta E}{15} \times \frac{\Delta - \delta E}{0.8\Delta - \delta E} \quad (1)$$

$$E(^4A_2) = 3A - 15B - 12Dq \quad (2)$$

$$E(^2E) = 3A - 6B + 3C - 12Dq \quad (3)$$

where A, B and C (cm^{-1}) are parameters of the interelectron interaction; $\delta E = \lambda_{ex2} - \lambda_{ex1}$, ($cm^{-1}$) is the difference between band energy maxima in absorption (PL excitation) spectra in the "blue" (λ_{ex2}, the $^4T_1 \rightarrow {}^4A_2$ transition) and "green" (λ_{ex1}, $^4T_2 \rightarrow {}^4A_2$ transition) regions; Δ (cm^{-1}) is the parameter of crystal field strength (10Dq) represented by the band energy maximum in absorption (PL excitation) spectra in the "green" region (λ_{ex1}, the $^4T_2 \rightarrow {}^4A_2$ transition).

Values of the parameters for (1) - (3) were found from PL and

PLE spectra of samples L-1 – L-4. Results of the calculation are listed in Table 5.

Table 5. Crystal field parameters for L-1 – L-4 samples

Sample	Δ , λ_{ex1}, $^4T_2 \rightarrow {}^4A_2$ /cm^{-1}	$\lambda_{ex.2,}$ $^4T_1 \rightarrow {}^4A_2$ /cm^{-1}	B / cm^{-1}	δE / cm^{-1}	Dq/B	C / cm^{-1}	C/B	β = B/B*`
L-1 (γ-Al_2O_3)	17 377	22 375	463	4 998	3.75	3 409	7.4	0.5
L-2 (γ*-Al_2O_3)	17 740	23 200	512	5 460	3.46	3 240	6.3	0.57
L-3 (α-Al_2O_3)	17 923	24 285	615	6 362	2.91	2 958	4.8	0.67
L-4 (α*-Al_2O_3)	17 825	24 418	643	6 593	2.77	2 874	4.5	0.7
Ruby single crystal	17 933	24 573	649	6 640	2.76	2 856	4.4	0.71
Ruby single crystal[13]	18 150	25 730	770	7 580	2.36	2 493	3.2	0.84

B* = 918 (cm^{-1}) is the parameter of interelectron interaction of a free ion, as determined from the atomic spectra.[26]

Data of Table 5 illustrate changes in the crystal field parameters Δ and B in a series from L-4 to L-1. Such a behavior of Δ indicates differences in the local surroundings of chromium ions for each sample, in particular L-1 and L-2. The Δ value decreases in a series from L-4 to L-1, thus testifying to an increase in the Cr – O distances with respect to the Cr – O distance in the ruby single crystal. Disagreement in the Δ values for single crystals is indicative of their degree of perfection, for example, the content of point defects represented by cationic and anionic vacancies. Table 5 shows also a decrease in the value of parameter B, which indicates a lowering of the interelectronic repulsive force between d electrons in a series from L-4 to L-1.

Crystal field strength reflects not only the electrostatic interaction of charges but also the effect of p – d bonds (anion – cation). The obtained values of C and C/B actually reveal changes in the Cr^{3+} bonding with the surroundings. A decrease in the interelectronic repulsion extends the cloud of d electrons, which is commonly related to the covalence effects. The degree of covalence is characterized by a ratio of the Racah parameter B and parameter of interelectron interaction of a free ion B*, β = B/B*.[26] In our case, the β value changes almost by 60% when passing from single crystal to L-1 sample. The resulting value is much greater than 40%, which is obtained for the elements with 3d electrons upon complexation.[26] The high value of the β parameter for the samples under study may be caused by the interaction between Cr^{3+} ions and OH groups, which concentration strongly differs for L-1 and L-2.

What about the molecular water sorbed on the alumina surface its role as the role of surface OH-groups is likely to lead to shape distortion of the PL spectrum. Molecular water and OH groups are known to have an intense absorption in the green-red region of the spectrum. The corresponding transitions lead from the ground energy level to the excited vibrational states of the same level. The presence of such absorption should be accompanied by "cutting out" the band corresponding to the $^4T_2 \rightarrow {}^4A_2$ (Cr^{3+}) transition from the long-wave region of the excitation spectrum. This is a possible reason why a shift of this band to the long-wave region is not observed, although such a shift is typical of the chromium ion behavior in the low-symmetry fields.[27]

Another possible reason of the high covalence is the interaction of chromium ion with nanodefects. As noted in[28], low-temperature aluminas should be classified with respect to their nanostructural features. For spinels, the distinctions between alumina phases may be related to their nanostructure, in particular, the morphology and linking of nanoparticles that have similar crystal structures[28]. It cannot be ruled out that for 3D nanolayers the position of energy levels responsible for the absorption can be exactly in the region of $^4T_2 \rightarrow {}^4A_2$ (Cr^{3+}) transition. Such assumption explains also the differences in PL properties of L-1 and L-2.

The unit cell volume for L-1 sample is smaller than that for L-2. On the contrary, the field strength Δ is characterized by a lower value for L-1 (Table 5). The latter additionally demonstrates that each of PLE spectra for samples L-1 and L-2 can be a superposition of two different spectra corresponding to two types of chromium luminescence sites.

In our study, the luminescence of chromium was recorded for the Cr^{3+} charge state, which was used to estimate the chromium content in L-1 and L-2 samples. However, after calcination of these samples, as seen from Table 3, chromium concentrations in L-3 and L-4 are strongly different. The concentration of Cr^{3+} chromium in L-1 and L-2 samples is 0.4×10^{-4} and 2.1×10^{-4}, respectively. Thus, some part of chromium in L-1 and L-2 does not produce the luminescence. In these samples, chromium is in octahedral and tetrahedral positions, with no luminescence for tetrahedral positions. After heat treatment of γ-Al_2O_3 to α-Al_2O_3, all the Cr^{3+}_{Td} positions become octahedral. In this connection, one can observe "an increase" in the Cr^{3+}_{Oh} concentration in α-Al_2O_3.

The ratio of Cr^{3+}_{Oh} concentrations for samples L-3 and L-1 is 4.8, while for L-4 and L-2, 4.7. The difference in Cr^{3+}_{Oh} concentrations for these pairs of samples is 1.5×10^{-4} and 7.7×10^{-4} wt.%, respectively. The difference in concentrations appeared to be greater than the Cr^{3+}_{Oh} concentration in the starting L-1 and L-2 samples. This formally indicates that the number of tetrahedral nonradiating positions exceeds the number of octahedral sites, which is unlikely. The contradiction is partially resolved by taking into account the growth in PL intensity after the calcination due to an increase in the quantum yield of the luminescence. In addition, the presence of chromium in other charge states, for example Cr^{6+} in L-1 and L-2 also cannot be excluded. Most likely, all these opportunities are implemented in samples L-1 and L-2.

As noted above, one of the structural differences between L-1 and L-2 is the ratio of tetrahedral cationic positions to octahedral ones, Td/Oh. Assuming a correct attribution of the luminescence

bands in L-1 and L-2 and neglecting changes in the PL quantum yield and bulk density of the samples, this ratio can be estimated for each sample. A ratio of the area under the Gaussian responsible for PL of Fe^{3+} ions to the total area of the Gaussians responsible for PL of Cr^{3+} characterizes the Td/Oh ratio. It is equal to 1 and 0.3, respectively, for L-1 and L-2. These ratios qualitatively agree with the ^{27}Al NMR data obtained by one of the authors of this paper for other AO samples. According to ^{27}Al NMR (MAS) data[17], crystal γ-Al_2O_3 is formed upon calcination of BE at 550-650 ºC for some hours. In the resulting γ-Al_2O_3, the Al^{3+} cations are in tetra- and octahedral positions. The cationic vacancies are related mostly to the Al^{3+}_{Oh} oxygen sites, which corresponds to a theoretically derived formula $Al_8[\square_{2.67}Al_{13.33}]O_{32}$. Therewith, for the γ-Al_2O_3 sample, the I_{AlTd}/I_{AlOh} ratio of line intensities is equal to 0.7, which virtually coincides with the theoretical ratio $I_{AlTd}/I_{AlOh} = 0.6$. According to ^{27}Al NMR data, the line intensity ratio for the P/BE γ*-Al_2O_3 phase is $I_{AlTd}/I_{AlOh} = 0.4$.[17]

Further analysis assumes that the samples under consideration have a low content of chromium, it does not form a solid solution, has a uniform statistical distribution over the volume and is located mostly in octahedral positions. Each of the L-1 and L-2 samples has two types of luminescence sites with the corresponding emission bands (Gaussians): λ_{a1} = 694.7 nm and λ_{b1} = 709 nm for L-1; λ_{a2} = 697.8 nm and λ_{b2} = 710.6 nm for L-2.

A position of each of the PL bands with respect to the emission band for L-3, L-4 and single crystals characterizes the extent of distortions of the octahedron surrounding the chromium ion. A greater shift toward higher wavelengths corresponds to a decrease in the crystal field strength. According to HRTEM data (Fig. 3), L-1 and L-2 samples differ from each other in the morphology, size and internal microstructure of the crystallites. The emission bands at λ_{b1} = 709 nm and λ_{b2} = 710.6 nm are very close for L-1 and L-2. This suggests that the corresponding octahedra are distorted to the same extent irrespective of the crystallite size. Such quite similar sites in L-1 and L-2 may be represented by the octahedra that are located in subsurface layers of the crystallites. The luminescence sites with the bands at λ_{a1} = 694.7 nm in L-1 and λ_{a2} = 697.8 nm in L-2 are the bulk ones. A shift of these bands to the long-wave region depends on the crystallite size, or more exactly, on the surface – bulk ratio. The smaller is the crystallite, the stronger is the distortion of the chromium ion surroundings, and the greater is the shift of PL band toward low energies. This reasoning agrees with the X-ray diffraction data on the morphology of the samples. A ratio of the Gaussian areas in L-1, $S(\lambda_{b1} = 709\ nm)/S(\lambda_{a1} = 694.7\ nm)$, is approximately equal to 6. For L-2, $S(\lambda_{b1} = 710.6\ nm)/S(\lambda_{a1} = 697.8\ nm) \approx 3.5$. Thus, according to luminescence data, the crystallites in L-1 are more coarse as compared to those in L-2. As noted above the L-1 and L-2 samples are lamellar materials with different unit cell volumes and specific surface areas. The difference in specific surface areas is directly related to the presence of layers with different thickness in L-1 and L-2. Each layer can be considered as a nanodefect whose energy levels are located in the band gap. A well-developed system of such layers and the impurity chromium ions produce the observed differences in the luminescence between L-1 and L-2 samples of the γ-Al_2O_3 phases. The presence of such electronic and geometrical structures suggests the existence of interrelation between the luminescence and catalytic properties of γ-Al_2O_3 phases.

Conclusions

The application of various physicochemical methods made it possible to reveal differences in the composition, unit cell volume, morphology, structure and specific surface area of the alumina γ-phases synthesized from BE and nanodispersed P/BE. Depending on the precursor substance, properties of the alumina γ-phase strongly differ with respect to some characteristics. In the tested alumina samples, the photoluminescence of Cr^{3+} and Fe^{3+} in their natural impurity concentrations was detected. The local structure of the synthesized aluminas was investigated using the Cr^{3+} and Fe^{3+} ions to find the crystal field strengths and Racah parameters for the γ-Al_2O_3 phases. A ratio of octahedral (Cr^{3+}) and tetrahedral (Fe^{3+}) cationic positions in each of the gamma phase samples was found to agree well with the ^{27}Al NMR data. The effect of residual bulk and surface OH groups on the local structure of γ-Al_2O_3 phases was revealed. For each phase, the luminescence of Cr^{3+} was detected in the subsurface structures. The presence of nanodefects, represented by the layers of interconnected crystallites, affects the electronic and spatial structures of γ-Al_2O_3 phases and shows up as the luminescence of probe ions. The use of Cr^{3+} and Fe^{3+} luminescence probes, which are present as concomitant impurities with low concentrations, makes it possible to exclude a special modification of alumina samples and investigate the system without introducing the additional distortions in the substance structure.

Acknowledgements

This research was performed under the UNIHEAT project. The authors wish to acknowledge the Skolkovo Foundation and BP for financial support. Also, the study was supported by the Russian Foundation for Basic Research (Project No. 14-03-31704 young_a) and was partially supported by the Russian Foundation for Basic Research (Project No. 13-03-00312 a).

Notes and references

[a] *Boreskov Institute of Catalysis, pr. Lavrentieva 5, Novosibirsk 630090, Russia. E-mail: rastorg@catalysis.ru*
** Corresponding author: A. Rastorguev (rastorg@catalysis.ru)*

1 B.C. Lippens, J.J. Steggerda, B.G. Linsen, Acad. Press. London, 1970, **4**, 232.
2 S.Y. Wilson, J. Solid State Chem., 1979, **30**, 247.
3 A.B. Stiles. Supports and Supported Catalysts. Khimiya, Moscow, 1991, 232.
4 R.S. Zhou, R.L. Shyder, Acta Crystallogr., 1991, **47**, 617-630.
5 K.I. Shefer, S.V. Cherepanova, E.M. Moroz, E.Yu. Gerasimov, S.V. Tsybulya, Journal of Structural Chemistry, 2010, **51**, 137-147.
6 E.M. Moroz, K.I. Shefer, D.A. Zyuzin, A.S. Ivanova, E.V. Kulko, V.V. Goidin, V.V. Molchanov, React. Kinet. Catal. Lett., 2006, **87**, 367-375.
7 E.M. Moroz, D.A. Zyuzin, K.I. Shefer, L.A. Isupova, Journal of Structural Chemistry, 2007, **48**, 754-756.
8 D. M. Lipkin, H. Schaffer, F. Adar, D.R. Clarke. Appl. Phys. Lett., 1997, **70**, 2550.
9 G. T. Pott & W. H. J. Stork, Catalysis Reviews: Science and Engineering, 1975, 163-199.

10 A.B. Kulinkin, S.P. Feofilov, R.I. Zakharchenya, Physics of the Solid State, **42**, 2000, 857–860. Translated from Fizika Tverdogo Tela, **42**, 2000, 835–838.

11 V.N. Snytnikov, V.O. Stoyanovskii, T.V. Larina, O.P. Krivoruchko, V.A. Ushakov, and V.N. Parmon, Kinetics and Catalysis, 2008, **49**, 291–298.

12 L. Trinkler, B. Berzina, Z. Jevsjutina, J. Grabis, I. Steins, C.J. Baily, Optical Materials, **34**, 2012, 1553–1557.

13 L. Trinkler, B. Berzina, D. Jakimovica, J. Grabis, I. Steins, Optical Materials, **33**, 2011, 817–822.

14 L. Trinkler, B. Berzina, D. Jakimovica, J. Grabis, I. Steins, Optical Materials, **32**, 2010, 789–795.

15 A.A. Rastorguev, M.G. Baronsky, N.A. Zaitseva, L.A. Isupova, A.I. Kostyukov, T.V. Larina, N.A. Pakhomov, V.N. Snytnikov, Inorganic Materials: Applied Research, 2014, **5**, 476–481. Translated from Perspektivnye Materialy, 2014, 11–17.

16 D.T. Sviridov, R.K. Sviridova, Yu. F. Smirnov, Optical spectra of transition metal ions in crystals. Nauka, Moscow, 1976, 266 p.

17 V.M. Mastikhin, O.P. Krivoruchko, V.I. Zaikovskii, R.A. Buyanov, React. Kinet. Catal. Lett., 1981, **18**, 117.

18 O.P. Krivoruchko, L.M. Plyasova, B.P. Zolotovskii, R.A. Buyanov, React. Kinet. Catal. Lett., 1983, **22,** 375.

19 G.N. Kryukova, V.I. Zaikovskii, L.M. Plyasova, O.P. Krivoruchko, B.P. Zolotovsky, R.A. Buyanov, Bulletin of the Siberian Branch of the USSR Academy of Sciences, 1984, **5**, 61.

20 V. B. Mikhailik, P. C. F. Di Stefano, S. Henry, H. Kraus, A. Lynch, V. Tsybulskyi, M. A., Journal of Applied Physics, 2011, **109**, 053116.

21 E.I. Nemykina, N.A. Pakhomov, V.V. Danilevich, V.A. Rogov, V.I. Zaikovskii, T.V. Larina, and V.V. Molchanov, Kinetics and Catalysis, 2010, **51**, 898–906.

22 G.T. Pott, B.D. McNicol, Chemical Physics Letters, 1970, **6**, 623-625.

23 D. Reinen, Structure and Bonding, Springer Verlag Berlin, 1969, **6**, 30-51.

24 C.J. Ballhausen, Introduction to Ligand Field Theory. Mir, Moscow, 1964, 360 p.

25 I. B. Bersuker, Electronic Structure and Properties of Transition Metal Compounds: Introduction to the Theory, 2nd Edition. Wiley 2010, 759 p.

26 J. Lewis, R.G. Wilkins. Modern coordination chemistry. Principles and methods, New York, 1960, 487 p.

27 G. Paglia, C.E. Buckley, A.L. Rohl, B.A. Hunter, R.D. Hart, J.V. Hanna, L.T. Byrne, Phys. Rev. B, 2003, **68**, 144110-1-144110-4.

28 S.V. Tsybulya. Dr. Sci. Thesis (phys.-math.), Novosibirsk, 2004.

Table of Contents

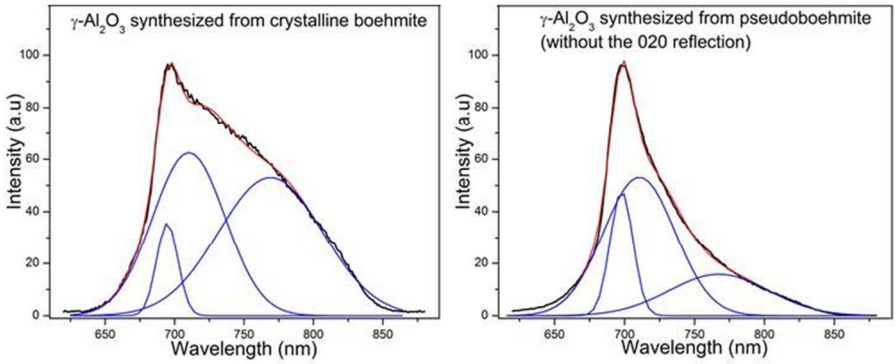

The differences between single-phase γ-Al_2O_3 powders synthesized from crystalline boehmite (BE) and pseudoboehmite (P/BE) (without the 020 reflection) are shown by PL method with the use of Cr^{3+} and Fe^{3+} luminescent probes present of the concomitant impurity.